Efficient Radiative and Nonradiative Energy Transfer from Proximal CdSe/ZnS Nanocrystals into Silicon Nanomembranes

Hue M. Nguyen,[†] Oliver Seitz,[‡] Weina Peng,[‡] Yuri N. Gartstein,[†] Yves J. Chabal,[‡] and Anton V. Malko[†,*]

[†]Department of Physics and [‡]Department of Materials Science, The University of Texas at Dallas, Richardson, Texas 75080, United States

Thin (few micrometers) and ultrathin (below 1 μm) film photovoltaic (PV) devices are emerging candidates for the low-cost replacement of thick, wafer-based solar cells. Manufacturing of thin-film devices is less expensive due to the reduced cost of raw materials and increased production throughput due to faster deposition times as especially applied to Si structures. Moreover, for semiconductors that are not surface recombination limited,[1] the use of thin layers leads to higher open-circuit voltages due to decreased bulk recombination. Further benefits include compatibility with lightweight, flexible substrates that potentially allow roll-to-roll production capabilities. However, the main limiting requirement for the device thickness is light absorption: thin-film PV devices must achieve the full absorption of the solar spectrum and be optically "thick" for wavelengths above the absorption edge of the semiconductor or otherwise employ enhanced light collection schemes.

Energy transfer (ET)-based hybrid nanostructures is an interesting class of materials potentially offering a versatile platform for various optoelectronic applications.[2,3] One component of such a hybrid is characterized by its strong light—matter interaction and the other by its high charge-carrier mobilities. The electromagnetic interaction is responsible for interconversion of neutral excitations, excitons, and electron—hole pairs between the components. In the PV mode of operation, incident light is efficiently harvested in the strongly absorbing component followed by exciton diffusion and ET across the interface with the subsequent separation and transport of charge carriers entirely within the high-mobility semiconductor (SC) component. Hybrid architectures operating on ET

ABSTRACT
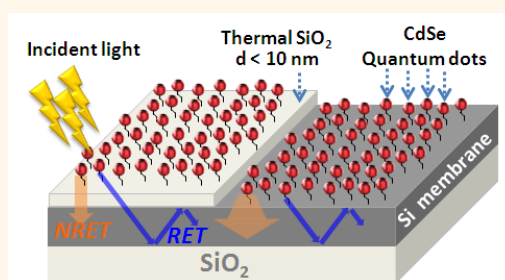
We demonstrate efficient excitonic sensitization of crystalline Si nanomembranes *via* combined effects of radiative (RET) and nonradiative (NRET) energy transfer from a proximal monolayer of colloidal semiconductor nanocrystals. Ultrathin, 25—300 nm Si films are prepared on top of insulating SiO$_2$ substrates and grafted with a monolayer of CdSe/ZnS nanocrystals *via* carboxy-alkyl chain linkers. The wet chemical preparation ensures that Si surfaces are fully passivated with a negligible number of nonradiative surface state defects and that the separation between nanocrystals and Si is tightly controlled. Time-resolved photoluminescence measurements combined with theoretical modeling allow us to quantify individual contributions from RET and NRET. Overall efficiency of ET into Si is estimated to exceed 85% for a short distance of about 4 nm from nanocrystals to the Si surface. Effective and longer-range radiative coupling of nanocrystal's emission to waveguiding modes of Si films is clearly revealed. This demonstration supports the feasibility of an advanced thin-film hybrid solar cell concept that relies on energy transfer between strong light absorbers and adjacent high-mobility Si layers.

KEYWORDS: hybrid nanostructures · thin film solar cells · energy transfer · silicon nanomembranes · colloidal nanocrystals

principles should be contrasted with more conventional charge transfer (CT)-based PV composites. CT-based devices rely on the exciton fission at the interface resulting in charge carriers on its different sides,[4] thus placing strong demands on carrier mobilities in both components as well as on the microscopic quality of the interface.

Nanostructured ET hybrids may provide an attractive direction for fabrication of

devices incorporating ultrathin Si layers as their high-mobility SC component. In such devices, Si films will be effectively sensitized *via* ET from strongly absorbing layers of organic molecules or inorganic nanocrystal quantum dots (NQDs). Consequently, the issue of the weak absorption in indirect band gap Si will no longer be a defining factor in determination of the device thickness. Provided that the efficacy of relevant ET processes can be maintained throughout, it is conceivable that efficient Si-based PV devices could be built with the overall thickness below 1 μm.

As a step toward that goal, in this paper, we report on spectroscopic evidence for efficient ET from an optically excited monolayer of colloidal CdSe/ZnS nanocrystals covalently grafted on thin (~100 nm) Si nanomembranes at well-defined distances. Our results demonstrate that ET into ultrathin Si layers can be as efficient as ET into bulk Si substrates.[5] We are able to quantitatively identify both nonradiative (NRET) and radiative (RET) energy transfer processes. The former, Förster-like,[3,6] process can be thought of as direct excitation[7] of the electron—hole pairs in Si by the electric field of the NQD excitons. In RET, on the other hand, the NQD exciton can decay into spatially confined, waveguiding, photonic modes[6] propagating *within* the Si nanomembrane parallel to its surface. These propagating modes would eventually be absorbed to produce electron—hole pairs and enhance the device performance. Our measurements confirm that NRET is a long-ranged, as compared with CT (few nanometers *vs* angstrom), process and show that RET is even longer-ranged. RET is able to couple NQD excitations to Si nanomembranes from tens of nanometers distances. Coupling to waveguiding modes exhibits a characteristic oscillatory behavior as a function of the membrane thickness and can account for a nearly 70% contribution to NQD radiative decay rates. For NQDs grafted on Si nanomembranes with optimal thicknesses, both ET processes can result in more than 85% of all NQD excitations to be transferred into Si. In this sense, Si nanomembranes serve as efficient energy acceptors and may be used as a materials system for flexible PV devices.

Out of the two types of ET that we explore, the idea of external NRET sensitization of inorganic SCs for PV applications was likely first discussed by Dexter,[8] which was shortly followed by more elaborate theoretical calculations[7] and experimental studies of NRET from molecular species into semiconductors.[9,10] Much more recently, this idea received a fresh boost with the help of colloidal NQDs as a new type of the sensitizer.[5,11−13] Nanocrystal quantum dots possess attractive photophysical properties: they have size-dependent band gaps that allow easy tuning of their photoluminescence (PL) emission wavelength, large absorption cross sections, and are exceptionally photostable as compared to organic media. It has been reported that a 6-fold enhancement of the photocurrent for patterned GaAs structures is achieved when covered with CdSe/CdS NQDs.[12] Justification of NRET into Si-based materials from NQDs has also attracted recent attention.[5,13]

It is interesting to put the idea of another ET process, RET sensitization, in the context of a newly emerging route toward more efficient PV devices which focuses on increasing the incident light absorption in thin SC layers with the help of metallic structures (see, for example, ref 14 and references therein). Plasmonic-assisted thin-film solar cells typically consist of thin layers of SC material with the plasmonic light-trapping patterns built into the metallic contacts. Various metallic nanostructures[15] provide different degrees of plasmonic-assisted absorption in active SC media due to the scattering-mediated local light trapping and locally enhanced electric fields. A number of experiments have also shown an increased absorption due to propagating surface plasmon modes[16] in the vicinity of metallic contacts. Finally, some plasmonic device geometries include coupling of the incident light into the waveguiding modes of the SC layer. RET coupling that we discuss here effectively acts similarly by converting the plane-wave incident light into waveguiding Si layer modes, albeit not *via* the scattering but *via* the absorption in NQDs and subsequent re-emission from the relaxed localized excitons. This type of configuration may have an important advantage: NQDs typically have high (~90%) PL quantum yields and long radiative lifetimes (10s of ns), thus potentially allowing for transfer of nearly all of the NQD excitations into the proximal SC layer.

RESULTS AND DISCUSSION

In our experiments, we focus on time-resolved PL studies from a monolayer of NQDs proximal to Si nanomembranes by measuring PL decay rates. It is then important to outline major features of the effects of this proximity on the decay rate (Γ) of an individual electric dipole emitter as expected from theoretical considerations. Fundamental understanding of manifestations of NRET and RET in different environments can be achieved already within a classical macroscopic electrodynamics picture of the fields of an oscillating dipole, with the media characterized by their frequency-dependent complex dielectric functions $\varepsilon(\omega) = \varepsilon'(\omega) + i\varepsilon''(\omega)$. Stemming from Sommerfeld's treatment[17] of an oscillating dipole above a semispace, a very comprehensive macroscopic description has been worked out for dipoles in different geometries that compares well to experimental data.[6,18,19] The results for classical dipoles are identical to those obtained in the quantum picture of the exciton decay due to fluctuations of the electromagnetic field (section 8.4 of ref 6). Particularly simple expressions are derived for stratified media as summarized in succinct reviews.[6,18] The decay rate of a dipole in a layered dielectric
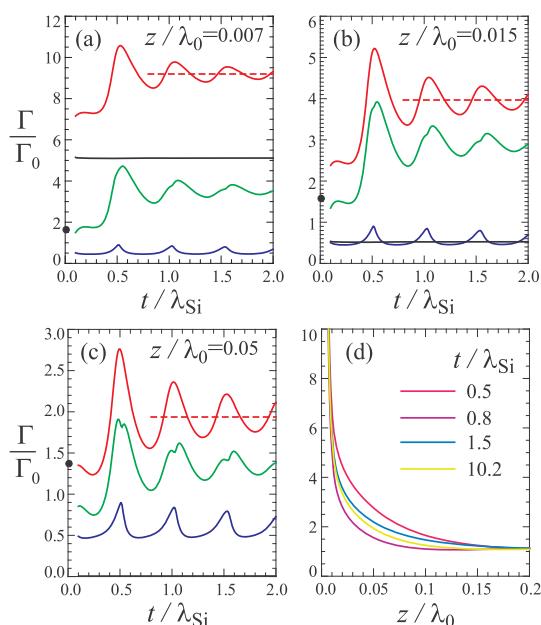
Figure 1. Model decay rates, in units of Γ_0, of a randomly oriented point-like electric dipole emitter at distance z from a free-standing Si layer. The dielectric function of Si used here for calculations is $\varepsilon = 16 + 0.25i$. (a–c) Decay rates as a function of the layer thickness t and differ by the distance to the layer, as measured in vacuum wavelengths λ_0: (a) $z = 0.007\lambda_0$, (b) $z = 0.015\lambda_0$, (c) $z = 0.05\lambda_0$. The layer thickness is measured in the wavelengths in Si, $\lambda_{Si} = \lambda_0/4$. The solid red lines depict the total decay rate as expressed by eq 4. The contributions to this total rate are displayed as follows: green lines for Γ_{RET} from the excitation of waveguiding modes in Si (eq 6), blue lines for Γ_v from the excitation of vacuum photons (eq 5), and black lines for Γ_{NRET} from NRET into Si (eq 7). The benchmark results for the total decay rate in the vicinity of the bulk Si substrate are shown as red dashed line levels and in the vicinity of the glass substrate as black dots. (d) Dependence on distance z for several values of the layer thickness as indicated. NRET is the major contributor to Γ at distances smaller than $\sim 0.01\lambda_0$, while RET dominates at larger separations up to $\sim 0.01\lambda_0$.

environment depends on its orientation; as appropriate for spherical NQDs, here we restrict our attention to results of equation (10.26) of ref 6 averaged over random dipole orientations. If the natural radiative decay rate of the dipole in vacuum is Γ_0, when positioned at distance z above a layered dielectric system, its electromagnetic decay rate is modified to Γ, with their ratio being equal to

$$\Gamma/\Gamma_0 = 1 + I(0, \infty) \qquad (1)$$

$$I(a, b) = \mathrm{Re} \int_a^b \frac{s\,ds}{2\sqrt{1-s^2}} [(2s^2 - 1)r^{(p)}(s) + r^{(s)}(s)]\exp(2ik_0 z\sqrt{1-s^2}) \qquad (2)$$

Here $r^{(s)}$ and $r^{(p)}$ are the reflection coefficients (from the whole structure) for, respectively, s- and p-polarized waves.[6] The information on the dielectric environment is contained in these reflection coefficients. As is known from standard treatments of the reflection/refraction at the planar interface problem, the in-plane (parallel to the

interface) components of the wave vector are conserved. The integration variable s in eq 2 actually relates magnitude $k_\parallel$ of those in-plane components to the vacuum wavenumber $k_0 = 2\pi/\lambda_0$ of the dipole emission at the transition frequency: $k_\parallel(s) = sk_0$. Consequently, the normal component of the wave vector k_{zi} in each of the layered spatial regions (index i) is determined by the value of the dielectric function ε_i of that layer:

$$k_{zi}^2(s) = (\varepsilon_i - s^2)k_0^2 \qquad (3)$$

Splitting the whole integration range in eq 1 into parts corresponding to different values of ε_i thus allows one to distinguish between "propagating" (real k_{zi} values) and evanescent (imaginary k_{zi} values) character of the waves in the respective spatial regions.

Figure 1a–c displays the calculated dependence of the decay rate of a randomly oriented dipole emitter in the vicinity of a free-standing Si slab as a function of the slab thickness t for three different separations z of the dipole from the slab surface. Figure 1d focuses on the distance z dependence. For these calculations, we used constants $\varepsilon' = 16$ and $\varepsilon'' = 0.25$ which approximately correspond to Si dielectric function at 2.15 eV.[20] This simplified model example allows us to clearly illustrate all of the salient generic features, which would only be slightly affected numerically in more involved structures under the experimental study.

For our case of the weak absorption in the slab, $\varepsilon'' \ll \varepsilon'$, the overall integral in eq 1 can in fact be "cleanly" separated into contributions coming from physically different decay processes, we will define and denote them as

$$\Gamma = \Gamma_v + \Gamma_{RET} + \Gamma_{NRET} \qquad (4)$$

where

$$\Gamma_v/\Gamma_0 = 1 + I(0, 1) \qquad (5)$$

$$\Gamma_{RET}/\Gamma_0 = I(1, \sqrt{\varepsilon'}) \qquad (6)$$

$$\Gamma_{NRET}/\Gamma_0 = I(\sqrt{\varepsilon'}, \infty) \qquad (7)$$

The behavior of all of these contributors is also shown in Figure 1a–c. As is clearly seen from eq 3, the contribution of eq 5 corresponds to the decay into such electromagnetic modes that can propagate throughout the whole space, just undergoing refraction (and some absorption) due to the slab, and we would call them "vacuum photons". The contribution eq 6, on the other hand, corresponds to the electromagnetic modes that can propagate only inside the slab, and the fields of these modes are evanescent outside of the slab. These are of course waveguiding modes undergoing total internal reflection at the slab surfaces (Chapter 10 of ref 6). These two contributions are *radiative*: they exist even when $\varepsilon'' = 0$, and practically do not change much for small ε''. The contribution

eq 7 is, however, very different: it vanishes for $\varepsilon'' = 0$ and is practically proportional to ε'' for the small absorption. There are no propagating photonic modes corresponding to the range of variable s in eq 7, and it describes a purely *nonradiative* process due to the Joule losses[3] in the slab caused by the electrostatic-like near-field of the dipole. A close numerical inspection of the integrand in eq 2 confirms that integral eq 6 acquires its value from narrow regions around the poles corresponding to waveguiding resonances. The value of integral eq 7 is, however, due to contributions from a broad continuous range of variable s.

The decay into waveguiding modes (eq 6) thus describes RET into the Si slab from our dipole emitter; this is a primary process, and the waveguiding modes will then be eventually absorbed while propagating along the Si layer. NRET (eq 7), on the other hand, provides a channel for the direct excitation of electron–hole pairs in Si. While there is some absorption in Si due to vacuum photons, it certainly becomes even smaller for thin films or nanomembranes, and in the context of our focus, we rather consider Γ_v as due to photons that are emitted without being captured in the Si slab. Figure 1 clearly shows that, in those parameter ranges, ET into Si substantially dominates over a generally suppressed emission of vacuum photons. This domination is particularly drastic for smaller separations z from the Si surface, where the total efficiency of ET can reach 90%. At a dipole-to-surface separation distance z of about 4 nm (Figure 1a, $\lambda_0 = 560$ nm), the largest contribution to the decay comes from NRET, with RET being a close (in this example) second. NRET, however, is very sensitive to the distance (roughly $\propto (1/z^3)^{3,5,18}$ in the regime of $z \ll t$) as well as to the magnitude of ε''. It can be even more dominating for smaller z and larger ε''. At the same time, already at distance z about 9 nm (Figure 1b), NRET falls off to the level of vacuum photon emission and is not discernible in Figure 1c for $z \simeq 29$ nm. Being a relatively shorter-range process, NRET is practically independent of the layer thickness in the range shown. A discussion of model results for even thinner layers will be provided elsewhere.

RET maintains the dominance of ET into Si over longer distances. Even at $z \simeq 29$ nm, it is about twice as efficient as emission of vacuum photons. Figure 1d gives a perspective of the distance z dependence over a broader range of z values. The study of respective contributions to the total decay rate shows that RET becomes comparable to the vacuum photon emission roughly at approaching $z \simeq 0.1\lambda_0$, that is, yielding about 50% efficiency of ET from distances z on the order of 50 nm in this model example. As a function of the layer thickness t, the overall decay rate reflects the oscillations of RET related to the effective coupling to various waveguiding modes as is apparent from the approximate "quantization" of maxima in Figure 1a–c

at halves of the wavelength in Si (dipoles oriented parallel and perpendicular to the layer exhibit somewhat different maxima positions). It is apparent that these oscillations take place "around" the level that would be observed for a dipole in the vicinity of the Si bulk substrate (Si half-space). Only for extremely thin films, RET exhibits a noticeable drop. Understandably, in real samples, oscillations of RET may be diminished or even washed out due to fluctuations of system parameters. A similar diminishing effect may take place for very broad emission lines.

Figure 1d also clearly indicates that, at very small distances z, the overall decay rate is dominated by NRET; however, at distances slightly in excess of $z/\lambda_0 \simeq 0.01$, where RET is an essential contributor, the dependence becomes affected even by the thickness of the slab. We note in this regard that details of the distance dependence are generally strongly influenced by the specific system geometric and electrodynamic response parameters, affecting, among other things, numerical magnitudes of contributions from parallel and perpendicular oriented dipoles. Our case of positive dielectric ε' is thus quite different from the case of the dipole decay in the vicinity of metallic surfaces[18,19] with negative ε', with the latter being able to support surface plasmon modes. The dependence exhibited in the example of Figure 1d is largely a monotonic falloff in the region of our interest in this paper, and the well-known oscillating behavior[6,18] is small on this scale and seen at longer separations.

Our experimental investigation of NRET and RET into Si nanomembranes concerns studies of PL from a single monolayer of NQDs specifically grafted on Si and silicon oxide surfaces. Si nanomembranes are realized by the wet chemical etching of silicon-on-insulator (SOI) films, which are then grafted with a single uniform monolayer of CdSe/ZnS nanocrystals. Grafting of a self-assembled monolayer (SAM) is known to completely passivate the Si surface through Si–C bonding and to provide functional headgroups for the NQD attachment.[21−23] Moreover, such a linker-assisted deposition allows for a precise NQD positioning at the predetermined distance from the Si surface, thus ideally suited for ET studies. We prepare nanocrystal/Si samples in which NQDs are placed on Si nanomembranes of various thicknesses ($25 < t < 300$ nm) and at various distances from the Si surface by depositing thin ($0 < d < 11$ nm) interfacial spacer layers of SiO_2 on the top of Si nanomembranes. The layer thicknesses and their homogeneity have been assessed with standard ellipsometric measurements showing very good model fits. In addition, SEM images have been taken, confirming a high degree of homogeneity. By increasing the spacing, we are able to progressively eliminate the NRET decay channel for NQD excitations (see the discussion above) and thus quantitatively distinguish RET. The schematics of our nanostructures, an SEM cross-sectional image of a sample, and Atomic Force
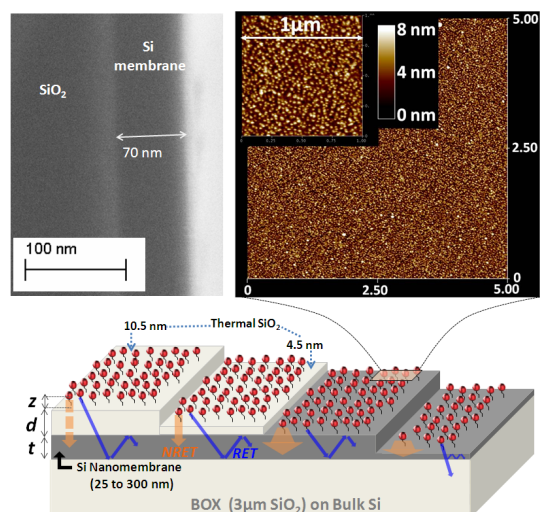
Figure 2. Different NQD/Si nanomembrane structures used to extract the relative participation of various decay channels: schematically displayed are NRET and RET processes from NQDs into the underlying Si slab as well as into SiO$_2$ substrate (on the rightmost structure). NRET role is strongly diminished with a thicker spacer (the leftmost structure), while the waveguiding modes in Si are excited quite efficiently. (Top left) SEM cross-sectional image of one of the experimental structures showing the uniformity of the Si membrane thickness. (Top right) AFM images of NQDs attached *via* carboxy-terminated alkyl chains on an oxide-free Si nanomembrane surface. The 5 × 5 μm image emphasizes the homogeneity of the NQDs' monolayer attachment, while the 1 × 1 μm confirms the individuality of the NQDs to minimize interdot ET effects.

Microscopy (AFM) images of the submonolayer surface coverage are shown in Figure 2. We also indicate on the figure the notations used throughout the paper for distances and thicknesses.

Figure 3 displays the time-dependent NQD photoluminescence (PL) decay results for a variety of samples studied. Panels of this figure are distinguished by the thickness of the oxide spacer layer on the top of the Si nanomembrane: no spacer ($d = 0$) in panel a, $d = 4.5$ nm in panel b, and $d = 10.5$ nm in panel c. Each of the panels features data for Si slabs of different thicknesses as indicated as well as the reference trace for the PL decay of NQD excitons on the bulk glass substrate. The trace for the glass substrate is well-characterized by a nearly monoexponential decay with the decay time $\tau_G \simeq 22.8$ ns, in agreement with our previous results.[5]

It is evident that decays of NQD excitons on the Si surface (Figure 3a) are much faster, with decay times τ ranging from 3.3 to 4.5 ns, depending on the Si film thickness. Here the decay times on Si were extracted from monoexponential fits in the 0−12.5 ns range. This fitting window was chosen because of the small (<5%) but noticeable presence of postpulses in the excitation power train due to the nonideal picking of the AO modulator. The first postpulse that appears at 12.6 ns after the main excitation pulse re-excites the NQDs and provides an upward "bump" in the PL traces, thus complicating numerical fits at longer times. Such re-excitation
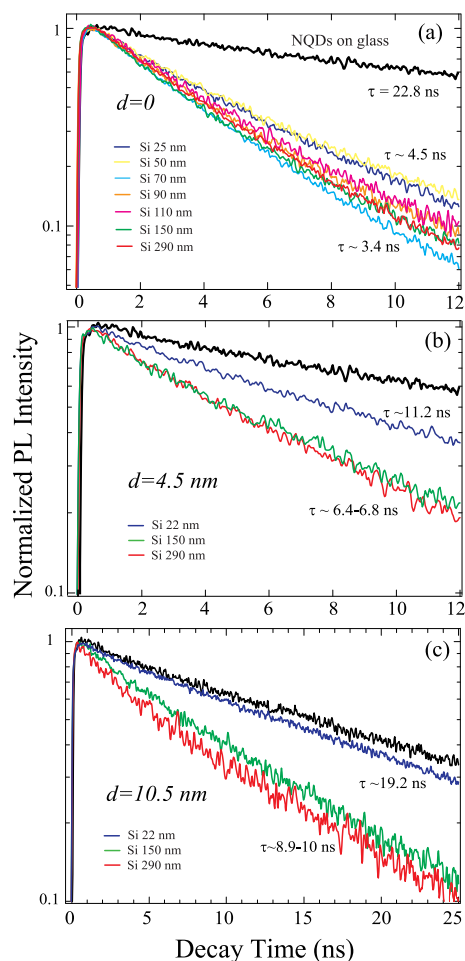

Figure 3. (a) PL dynamics for NQDs grafted on bare Si nanomembranes with thicknesses $t = 25$, 50, 70, 90, 110, 150, and 290 nm compared to NQDs on the reference glass substrate (top curve). Slowest dynamics measure decay time $\tau = 4.5$ ns and correspond to the NQDs on ultrathin ($t = 25$ and 50 nm) Si slabs. (b,c) Dynamics for NQDs grafted on $t = 22$, 150, and 290 nm Si slabs that have spacer layers of thermal SiO$_2$ of thicknesses $d = 4.5$ nm (b) and $d = 10.5$ nm (c) to increase the distance between NQDs and the Si surface.

events are not visible in slow decays but are noticeable in the NQD on Si decay curves due to shorter lifetimes and a nearly complete PL relaxation within the 12.5 ns window. (We also evaluate decay curves in the 0−25 ns range; these fits are later used to determine experimental errors in the data points shown in Figure 4a.) Additionally, some PL decays (including those on glass) have a small (≃10%) initial component that may be due to some trapping channels intrinsic to NQDs and are not included in the fits. It is also apparent in Figure 3b,c that decay times τ become progressively longer for larger separations of the NQDs from the Si surface as affected by the SiO$_2$ spacer layer between Si and grafted NQDs. These observed trends are well accounted for in the general qualitative picture of the contributions from NRET and RET into Si slabs that we discussed above.
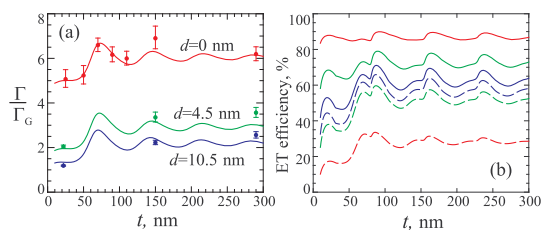
Figure 4. (a) Relative acceleration of the NQD exciton decay with respect to the reference glass sample as a function of the thickness t of the Si nanomembrane. The data points and theoretical curves are grouped by different values d of the silicon oxide spacer thickness. The distance of the dipole emitter from the top surface is taken as $z = 4$ nm for the red theoretical curve and $z = 3.7$ nm for the green and blue ones. The dielectric parameters of Si used for calculations are $\varepsilon' = 16.5$ and $\varepsilon'' = 0.32$. Here the data points are shown with the reference $\tau_G = 22.8$ ns. (b) Efficiency of ET *into* Si as extracted from the color-coordinated theoretical curves in panel a. The solid lines correspond to the total ET efficiency, ($\Gamma_{RET} + \Gamma_{NRET}$)/$\Gamma$; dashed lines show the relative efficiency of ET just *via* waveguiding modes in the Si nanomembrane, Γ_{RET}/Γ.

For a better appreciation of these trends and for a quantitative assessment, the decay times τ derived from the dynamics in Figure 3 are summarized in Figure 4a in the form of $\tau_G/\tau = \Gamma/\Gamma_G$ with respect to the reference glass sample. The experimental data points are plotted along with theoretical curves calculated according to eq 1 and eq 2. In these calculations, we employed $\lambda_0 = 560$ nm and the dielectric parameters of Si as $\varepsilon' = 16.5$ and $\varepsilon'' = 0.32$; these values are close to the tabulated data in ref 20 in this frequency range. A good correspondence between the experimental and theoretical data is quite compelling and indicates no need for possible further parameter variations. We note that we have not been pursuing this in the context of a numerical parametric fitting but rather as a faithful representation of salient experimental features and dependencies within the simplest theoretical framework.

As our experimental structures contain both Si and SiO_2 components (we take the refraction index of the latter as $n = 1.5$), the radiative decay products now contain those electromagnetic modes that can propagate in the SiO_2. The decay rate into Si waveguiding modes *per se* in these studied structures is then modified from eq 6 to

$$\Gamma_{RET}/\Gamma_0 = I(1.5, \sqrt{\varepsilon'}) \qquad (8)$$

One can now use the theoretical outputs in Figure 4a to extract the corresponding rates, eq 7 and eq 8, of ET processes from quantum dots *into* Si. We define the overall efficiency of ET into Si as a fraction of the *total* decay rate:

$$(\Gamma_{RET} + \Gamma_{NRET})/\Gamma \qquad (9)$$

The remainder of the decay takes place *via* emission of photons that propagate in vacuum and/or in the SiO_2, which we consider here as lost for ET under consideration. Efficiency eq 9 includes both NRET and RET into Si

nanomembranes. The RET fraction, corresponding to the decay into Si waveguiding modes, is given by Γ_{RET}/Γ. Figure 4b displays the extracted efficiency data. As expected, these data exhibit oscillating variations as a function of Si layer thickness t. To quote a single number for comparison purposes, we average theoretical results in the range of thicknesses between 70 and 300 nm.

Figure 4b then shows an estimated remarkable 87% efficiency of ET into Si from quantum dots grafted directly on the Si surface where distance $d + z$ from the NQD center to the surface is about 4 nm. At this distance, NRET dominates, accounting for 58%, while RET adds 29%. (The leftover 13% is "lost" to other decay channels.) The relative roles of NRET and RET progressively interchange as the distance to Si increases. The green curves in Figure 4b—for the distance of about 8.2 nm—yield a 52% efficiency of RET and 21% of NRET, making together 73% efficient ET. Finally, at the distance of about 14.2 nm (blue curves), overall ET efficiency of 63% is contributed to mostly by RET, accounting for 57.5%, whereas NRET becomes much smaller at 5.5%. With these theoretical estimates, the experimental results thus clearly indicate that overall ET from NQD into thin Si layers can be indeed as efficient as ET into thick Si substrates,[5] but without the expense of the latter. It is also clear that RET represents a major long-range mechanism by which NQD excitons can be transferred into the underlying thin semiconductor layer.

It is worth stressing that ET efficiencies, eq 9, should be distinguished from the absolute values of the decay rates, eq 6—eq 8, as the efficiency takes into account variations of the decay rates into other channels, as well. This is particularly clear in Figure 1, which shows modulations of Γ_v along with modulations of Γ_{RET}. Thus, the maxima of curves in Figure 4b deviate from maxima of curves in Figure 4a. While NRET rates are practically independent of the Si layer thickness t in the studied range, RET rates reflect the coupling strength to the Si waveguiding modes and therefore do depend on t (Figure 1). It should be noted that this coupling strength is expected to undergo a drop for extremely thin films, which is indeed what is observed in our experiments on the thinnest studied layers with thicknesses t of 25 and 50 nm (Figure 4a). The RET rate, however, quickly reaches its largest values already at $t \simeq 70$ nm, the expectation also recovered in our experimental data. It is also of interest to quantify the place of the coupling to Si waveguiding modes among the radiative decay processes only. One then immediately confirms that the emission of Si waveguiding modes dominates over emission of other types of photons in a wide range of parameters studied. When averaged over thicknesses $70 < t < 300$ nm, the fraction of waveguiding modes in the radiative emission content amounts to 69, 66, and 61%, respectively, for the red,

green, and blue data sets in Figure 4. Even for very thin t = 25 nm Si films, these fractions remain quite substantial: 59, 54, and 47% for the same data sets. We remind the reader that here we evaluate these efficiencies for the experimentally studied structures, with some emitted photons lost to the SiO_2 substrate. The relative efficiency of RET into Si would be even higher in structures without such losses, including the model example of Figure 1.

In the discussion of the relative roles of NRET and RET into the neighboring semiconductor (SC) film, it is important to realize that in the parameter range of practical interest, the efficiency of NRET is proportional to the absorption in the SC, that is, to the imaginary part ε'' of the dielectric function. RET, on the other hand, owes its efficiency to the high refraction index n of the SC, which corresponds to the real part ε'. While the refraction index of crystalline Si changes only slowly from the visible to the near-IR region of the spectrum, the absorption undergoes a much more substantial reduction. So, at $\hbar\omega$ = 2.2 eV (the region close to our current study), ref 20 quotes ε' = 16.3 (n = 4) and ε'' = 0.26, while at $\hbar\omega$ = 1.5 eV, the dielectric parameters of crystalline Si become ε' = 13.5 (n = 3.7) and ε'' = 0.04. We therefore expect RET to be an even more important channel in harvesting the near-IR portion of the solar spectrum with crystalline Si-based nanostructures, where the efficiency of NRET coupling is quite limited due to the strongly decreased Si absorption.

The radiative coupling of NQD excitons to waveguiding modes of thin Si films can be compared to the light coupling recently realized in plasmonic-assisted metal/organic and metal/semiconductor structures. Both surface plasmon modes that propagate along the metal surface and coupling of the incident light to the waveguiding modes via sub-micrometer-sized metal structures have been discussed (see ref 14 and references therein). We note that plasmonic excitations are inherently lossy, thus reducing the photon conversion efficiency. Being somewhat of the "wave diffraction" origin, coupling of the plane-wave incoming light to the waveguiding modes due to metallic substructures would typically have a pronounced wavelength dependence. Several recent publications describe scattering of incident photons by metal nanoparticles deposited on the back surface of a solar cell structure that enables light coupling to lateral propagation modes within the multiquantum well layer.[24,25] The coupling indeed was found to have a strong wavelength dependence and led to a relatively modest enhancement of the power conversion efficiency (by ~17%), suggesting that further improvements are necessary.

Our approach to the incident light conversion is in this regard very different. Given the broad absorption spectrum of semiconductor NQDs, all incident photons above the absorption edge are absorbed. The resulting relaxed excitons are then effectively transferred via NRET/RET into the Si waveguide. Our experiments show that waveguiding modes in the 2 eV frequency range are excited with high efficiency for Si layers with thicknesses as small as 70 nm and above. At the same time, RET is clearly demonstrated to be a much longer-range process than NRET. To our knowledge, the measurements in this paper are the first quantitative determinations of the radiative coupling of nanoscale emitters to the waveguiding modes in Si nanomembranes. The intrinsic efficiency of nearly 70% that we assess for the coupling to the waveguiding modes among the radiative channels is quite high and points to specific ways to improve the operation of thin-film PV structures.

In order to engineer practical ET-based thin-film PV devices, one has to maximize absorption of the incident light while maintaining high ET efficiency to the underlying semiconductor. The efficient light absorption requires NQD films of certain thicknesses estimated to be 200–300 nm. Several recent reports investigated the use of size-gradient NQD films with engineered energy flows between NQD layers from smaller NQDs (having larger band gaps) to larger ones (with smaller band gaps) accomplished via interdot Förster energy transfer.[26−29] Those studies reported effective transfer times between adjacent NQD layers on the order of hundreds of picoseconds, certainly much faster than the radiative lifetimes (tens of nanoseconds) reported for such NQDs. We envision that in conjunction with our demonstration of efficient energy transfer from proximal NQDs into Si layers, the strategy of the directed delivery could provide an effective way to convert the absorbed energy into excitations in Si. In another approach, various geometrical architectures could also be used in ET-based Si devices as we recently demonstrated with Si nanopillars.[30] Experimental studies of energy transfer in nanostructures with thick layered NQD films deposited on Si nanomembranes is an important direction of future pursuits.

We note that RET may also play an important role to efficiently extract excitations from so-called "giant" NQDs. This recently developed breed of multishell CdSe/CdS NQDs has attracted considerable attention due to their superior photophysical properties such as a completely nonblinking behavior, extreme photostability, and existence of the long-lived multiexcitonic states.[31−33] However, large CdS (up to 5 nm thick) shells used in such NQDs may prevent direct charge extraction and even hamper NRET into outside substrates, thereby limiting their possible optoelectronic applications. We expect that RET with its much longer-ranged nature can still be operational.

CONCLUSIONS

To summarize, we have performed a systematic study of energy transfer mechanisms from optically

excited CdSe/ZnS semiconductor nanocrystals covalently grafted on functionalized ultrathin (25–300 nm) crystalline Si nanomembranes. The monolayer preparation strategy allows us to quantify effects of nonradiative and radiative energy transfer *into* Si on NQD de-excitation pathways. Our experimental data indicate that overall ET efficiency may exceed 85% for proximal NQDs (distance from the Si surface about 4 nm) and can be as good on nanomembranes as on bulk Si substrates.[5] We have been able to distinguish contributions from NRET and RET whose relative roles vary depending on the distance from NQDs to Si. While short-distance ET efficiency is dominated by NRET, the data suggest that radiative

coupling of NQD excitons to Si waveguiding modes can be quite effective and is much longer-ranged than NRET. The excitation of waveguiding modes is estimated to constitute a 60–70% fraction of the radiative decay channels in the studied samples. In thin-film PV devices, these waveguiding modes will be eventually absorbed in Si, leading to an increased production of electron–hole pairs. Our observations support the development of NQD-sensitized, ultrathin Si film structures as candidates for PV devices with the performance exceeding the up-to-date limit and directly impacting the attainment of economically competitive renewable energy sources based on thin-film solar technology.

METHODS

Thin and ultrathin Si nanomembranes were processed from SOI wafers having a 300 nm initial thickness of the Si layer on the top of a 3 μm thick SiO_2 insulator (BOX SiO_2). When thermal oxidation of the top Si layer was employed in a clean room environment, the Si membrane thickness was reduced to a set of samples with different values of t: 290, 150, 110, 90, 70, 50, and 25 nm. Each of the samples was then split into several pieces, and a 1% HF etching solution was used to remove the desired amount of oxide to produce a series of samples with the identical thickness t of the Si layer but with different oxide thicknesses on its top: $d = 0$ (bare Si surface), $d = 4.5$, and $d = 10.5$ nm. Additionally, a reference sample with NQDs grafted on a glass coverslip slide was prepared. Surface functionalization is based on two approaches depending on the starting surfaces. For oxide-free Si surfaces, a hydrosilylation reaction using ethyl undecylenate molecules is performed, leading to a carboxylic-acid-terminated alkyl chain monolayer after transformation of the headgroups.[22] For silicon oxide (SiO_2) or pure glass surfaces, the freshly cleaned samples are immersed in a preheated (70 °C) anhydrous toluene solution containing 0.2% of triethoxysilyl undecanal (C11-Ald) molecules for 12 h in a recirculation glovebox (anhydrous conditions). Water-soluble colloidal NQDs emitting at $\lambda_0 \simeq 560$ nm are purchased from Invitrogen and used as received. The attachment of NQDs is performed differently depending on the headgroups: (a) for carboxyl-terminated headgroup, the sample is immersed in an MES (2-morpholinoethanesulfonic acid) solution containing EDC (1-ethyl-3-(3-dimethylaminopropyl)carbodiimide) (0.8 mg/mL) and with NQD concentration of 15 nM; (b) for aldehyde-terminated headgroup, the sample is exposed to an NQD solution containing some sodium cyanoborohydride (5 mM). The measured ellipsometric thicknesses of SAM molecules employed in these attachments are 1.5 nm and 2 ± 0.2 nm, resulting in the center of NQD to the top surface distances of approximately 3.7 and 4.2 nm, respectively. As described in our previous work,[5] these concentrations correspond to submonolayer NQD coverage in order to avoid interdot NRET effects that typically complicate data interpretation. The samples are left for 90 min for adsorption, rinsed at least twice with DI water, and dried under the N_2 gas. (For thin glass slides, a homemade holder is used to perform the adsorption only on one side of the slide.) The resultant structures and AFM image of the submonolayer surface coverage are shown in Figure 2.

For spectroscopic studies. we used a microscope-based time-resolved PL system. Samples were mounted on the microscope table and excited by 400 nm/120 fs optical pulses at 7.6 MHz repetition rate produced by doubling the fundamental frequency of the Mira 900 oscillator laser and followed by pulse-picking (1 out of 10 pulses) *via* the acousto-optical modulator (NEOS Technologies). Excitation was focused on the sample *via* NA = 0.6 objective that also ensured a high photon collection efficiency necessary to obtain PL signatures from a

submonolayer of NQDs. The collected emission was passed through a spectrometer and directed either to a CCD camera for spectral analysis or to a sensitive photon detector (MicroPhoton Devices) for the wavelength-dependent PL lifetime detection. PL decays were collected *via* the time-correlated single-photon counting (TCSPC) performed on board of Pico300E photon counting hardware (PicoQuant GmbH). The overall time resolution was better than 50 ps.

Conflict of Interest: The authors declare no competing financial interest.

REFERENCES AND NOTES

1. Campbell, P.; Green, M. A. The Limiting Efficiency of Silicon Solar Cells under Concentrated Sunlight. *IEEE Trans. Electron Devices* **1986**, *33*, 234–239.
2. Oulton, R. F.; Takada, N.; Koe, J.; Stavrinou, P. N.; Bradley, D. D. C. Strong Coupling in Organic Semiconductor Microcavities. *Semicond. Sci. Technol.* **2003**, *18*, S419–S427.
3. Agranovich, V. M.; Gartstein, Y. N.; Litinskaya, M. Hybrid Resonant Organic–Inorganic Nanostructures for Optoelectronic Applications. *Chem. Rev.* **2011**, *111*, 5179–5124.
4. Sun, S. S., Sariciftci, N. S., Eds. *Organic Photovoltaics: Mechanisms, Materials, and Devices*; CRC Press: Boca Raton, FL, 2005.
5. Nguyen, H. M.; Seitz, O.; Aureau, D.; Sra, A.; Nijem, N.; Gartstein, Y. N.; Chabal, Y. J.; Malko, A. V. Spectroscopic Evidence for Nonradiative Energy Transfer between Colloidal CdSe/ZnS Nanocrystals and Functionalized Silicon Substrates. *Appl. Phys. Lett.* **2011**, *98*, 161904/1–3.
6. Novotny, L.; Hecht, B. *Principles of Nano-Optics*; Cambridge University Press: Cambridge, 2006.
7. Stavola, M.; Dexter, D. L.; Knox, R. S. Electron–Hole Pair Excitation in Semiconductors *via* Energy Transfer from an External Sensitizer. *Phys. Rev. B* **1985**, *31*, 2277–2289.
8. Dexter, D. L. Two Ideas on Energy Transfer Phenomena: Ion-Pair Effects Involving the OH Stretching Mode, and Sensitization of Photovoltaic Cells. *J. Lumin.* **1979**, *18/19*, 779–784.
9. Whitmore, P. M.; Alivisatos, A. P.; Harris, C. B. Distance Dependence of Electronic Energy Transfer to Semiconductor Surfaces: Pyrazine/GaAs(110). *Phys. Rev. Lett.* **1983**, *50*, 1092–1094.
10. Alivisatos, A. P.; Arndt, M. F.; Efrima, S.; Waldeck, D. H.; Harris, C. B. Electronic Energy Transfer at Semiconductor Surfaces. I. Energy Transfer from Two-Dimensional Molecular Films to Si(111). *J. Chem. Phys.* **1987**, *86*, 6540–6549.

11. Lu, S.; Madhukar, A. Nonradiative Resonant Excitation Transfer from Nanocrystal Quantum Dots to Adjacent Quantum Channels. *Nano Lett.* **2007**, *7*, 3443–3451.

12. Chanyawadee, S.; Harley, R. T.; Henini, M.; Talapin, D. V.; Lagoudakis, P. G. Photocurrent Enhancement in Hybrid Nanocrystal Quantum-Dot p-i-n Photovoltaic Devices. *Phys. Rev. Lett.* **2009**, *102*, 077402/1−4.

13. Lu, S.; Lingley, Z.; Asano, T.; Harris, D.; Barwicz, T.; Guha, S.; Madhukar, A. Photocurrent Induced by Nonradiative Energy Transfer from Nanocrystal Quantum Dots to Adjacent Silicon Nanowire Conducting Channels: Toward a New Solar Cell Paradigm. *Nano Lett.* **2009**, *9*, 4548–4552.

14. Atwater, H. A.; Polman, A. Plasmonics for Improved Photovoltaic Devices. *Nat. Mater.* **2010**, *9*, 205–213.

15. Zhu, J.; Hsu, C.-M.; Yu, Z.; Fan, S.; Cui, Y. Nanodome Solar Cells with Efficient Light Management and Self-Cleaning. *Nano Lett.* **2010**, *10*, 1979–1984.

16. Ferry, V. E.; Sweatlock, L. A.; Pacifici, D.; Atwater, H. A. Plasmonic Nanostructure Design for Efficient Light Coupling into Solar Cells. *Nano Lett.* **2008**, *8*, 4391–4397.

17. Sommerfeld, A. *Partial Differential Equations in Physics*; Academic Press: New York, 1964.

18. Chance, R. R.; Prock, A.; Silbey, R. In *Advances in Chemical Physics*; Rice, S. A., Prigogine, I., Eds.; Wiley: New York, 1978; Vol. 37, pp 1−65.

19. Waldeck, D. H.; Alivisatos, A. P.; Harris, C. B. Nonradiative Damping of Molecular Electronic Excited States by Metal Surfaces. *Surf. Sci.* **1985**, *158*, 103–125.

20. Aspnes, D. E.; Studna, A. A. Dielectric Functions and Optical Parameters of Si, Ge, GaP, GaAs, GaSb, InP, InAs, and InSb from 1.5 to 6.0 eV. *Phys. Rev. B* **1983**, *27*, 985–1009.

21. Aureau, D.; Varin, Y.; Roodenko, K.; Seitz, O.; Pluchery, O.; Chabal, Y. J. Controlled Deposition of Gold Nanoparticles on Well-Defined Organic Monolayer Grafted on Silicon Surfaces. *J. Phys. Chem. C* **2010**, *114*, 14180–14186.

22. Seitz, O.; Dai, M.; Aguirre-Tostado, F. S.; Wallace, R. M.; Chabal, Y. J. Copper-Metal Deposition on Self Assembled Monolayer for Making Top Contacts in Molecular Electronic Devices. *J. Am. Chem. Soc.* **2009**, *131*, 18159–18167.

23. Seitz, O.; Fernandez, P. G.; Mahmud, G. A.; Wen, H.-C.; Stiegler, H. J.; Chapman, R. A.; Vogel, E. M.; Chabal, Y. J. One-Step Selective Chemistry for Silicon-on-Insulator Sensor Geometries. *Langmuir* **2011**, *27*, 7337–7340.

24. Derkacs, D.; Chen, W. V.; Matheu, P. M.; Lim, S. H.; Yu, P. K. L.; Yu, E. T. Nanoparticle-Induced Light Scattering for Improved Performance of Quantum-Well Solar Cells. *Appl. Phys. Lett.* **2008**, *93*, 091107/1−3.

25. McPheeters, C. O.; Hu, D.; Schaadt, D. M.; Yu, E. T. Semiconductor Heterostructures and Optimization of Light-Trapping Structures for Efficient Thin Film Solar Cells. *J. Opt.* **2012**, *14*, 024007/1−11.

26. Achermann, M.; Petruska, M. A.; Crooker, S.; Klimov, V. I. Picosecond Energy Transfer in Quantum Dot Langmuir−Blodgett Nanoassemblies. *J. Phys. Chem. B* **2003**, *107*, 13782–13787.

27. Franzl, T.; Klar, T. A.; Schietinger, S.; Rogach, A. L.; Feldmann, J. Exciton Recycling in Graded Gap Nanocrystal Structures. *Nano Lett.* **2004**, *4*, 1599–1603.

28. Lee, J.; Govorov, A. O.; Kotov, N. A. Bioconjugated Superstructures of CdTe Nanowires and Nanoparticles: Multistep Cascade Förster Resonance Energy Transfer and Energy Channeling. *Nano Lett.* **2005**, *5*, 2063–2069.

29. Rogach, A. L.; Klar, T. A.; Lupton, J. M.; Meijerink, A.; Feldmann, J. Energy Transfer with Semiconductor Nanocrystals. *J. Mater. Chem.* **2009**, *19*, 1208–1221.

30. Seitz, O.; Caillard, L.; Nguyen, H. M.; Chiles, C.; Chabal, Y. J.; Malko, A. V. Optimizing Non-radiative Energy Transfer in Hybrid Colloidal-Nanocrystal/Silicon Structures by Controlled Nanopillar Architectures for Future Photovoltaic Cells. *Appl. Phys. Lett.* **2012**, *100*, 021902/1−4.

31. Chen, Y.; Vela, J.; Htoon, H.; Casson, J. L.; Werder, D. J.; Bussian, D. A.; Klimov, V. I.; Hollingsworth, J. A. "Giant" Multishell CdSe Nanocrystal Quantum Dots with Suppressed Blinking. *J. Am. Chem. Soc.* **2008**, *130*, 5026–5027.

32. Malko, A. V.; Park, Y.-S.; Sampat, S.; Vela, J.; Chen, Y.; Hollingsworth, J. A.; Klimov, V. I.; Htoon, H. Pump-Intensity- and Shell-Thickness-Dependent Evolution of Photoluminescence Blinking in Individual Core/Shell CdSe/CdS Nanocrystals. *Nano Lett.* **2011**, *11*, 5213–5218.

33. Htoon, H.; Malko, A. V.; Bussian, D.; Vela, J.; Hollingsworth, J. A.; Chen, Y.; Klimov, V. I. Highly Emissive Multiexcitons in Steady-State Photoluminescence of Individual "Giant" CdSe/CdS Core/Shell Nanocrystals. *Nano Lett.* **2010**, *10*, 2401–2407.